Fuel 421 (2026) 138969

Contents lists available at ScienceDirect

Fuel

journal homepage: www.elsevier.com/locate/jfue

Full length article

Analysis of the overlap of devolatilisation and char conversion during single coal particle burning using a detailed multi-step kinetic approach

Tien Duc Luu [a,*], Ali Shamooni [b], Yichong Zhou [b], Andreas Kronenburg [b], Oliver T. Stein [a]

[a] Engler-Bunte-Institut (EBI), Simulation of Reacting Thermo-Fluid Systems (TFS), Karlsruhe Institute of Technology (KIT), Engler-Bunte-Ring 7, 76131 Karlsruhe, Germany

[b] Institute for Reactive Flows (IRST), University of Stuttgart, Pfaffenwaldring 31, 70569 Stuttgart, Germany

HIGHLIGHTS

- Detailed BLRS to investigate the interaction and overlap between devolatilisation and char conversion.
- Detailed multi-step kinetic approach to describe the coal particle conversion.
- Proposed a first-of-its-kind methodology and criteria to evaluate the overlap.
- Developed a regression for integration into reduced-order models.

ARTICLE INFO

Keywords:
Coal combustion
Devolatilisation
Char conversion
Multi-step kinetics
BLRS

ABSTRACT

The interaction and overlap between the devolatilisation and char conversion processes of a single coal particle are investigated using a detailed boundary layer resolved simulation (BLRS) approach, in which all relevant gradients are resolved and gas solid interactions are represented through a set of boundary conditions. The gas phase is modelled with a detailed homogeneous reaction mechanism comprising 76 species and 973 reactions. The solid phase is treated as a porous medium with a detailed multi-step kinetic approach for both devolatilisation and char conversion (CRECK-S-C). The devolatilisation mechanism includes 32 species and 35 reactions, while the char conversion mechanism involves 8 species and 14 reactions. In total, 45 simulations are performed under varying ambient conditions, i.e. oxygen concentration, gas temperature, and varying particle size. The overlap between devolatilisation and char conversion is quantified by a criterion where the respective conversion rates differ by less than one order of magnitude, indicating a strong coupling that should not be neglected. Moreover, the overlap is expressed as the fraction of volatile mass released when char conversion becomes significant, Y_{OL}, which can be directly applied in reduced-order models, e.g. sub-models in the Euler-Lagrange context. The results reveal a consistent trend for smaller particle sizes ($d_p \leq 100\,\mu m$). Increasing ambient temperature, oxygen concentration and/or particle diameter leads to earlier start of overlap, corresponding to a lower value of Y_{OL}. For larger particle sizes ($d_p > 100\,\mu m$) a slightly different behaviour has been observed, particularly under a certain condition, where larger overlap regions, i.e. lower Y_{OL} values, occur than would be expected from the general trend. Based on these findings, a linear regression model for $Y_{OL}(X_{O_2}, T, d_p)$ was derived to predict the activation point of char conversion sub-models under varying conditions that can be implemented in reduced-order simulations.

1. Introduction

To guarantee a secure energy supply in the next few decades, reliability and efficiency have highest priority. The conversion of solid fuels, in particular pulverised coal combustion (PCC), remains one of the most common and established technologies for generating baseload electrical power, due to its long-term proven operational reliability and well-established technical performance. However, the inherent pollution and greenhouse gases caused by PCC drive significant research efforts to gain a deeper understanding of its underlying thermochemical processes, including ignition and combustion behaviour, in order to mitigate pollution and climate change. During PCC, a solid fuel particle generally undergoes five main thermo-physical stages [1], namely:

* Corresponding author.
Email address: tien.luu@kit.edu (T.D. Luu).

https://doi.org/10.1016/j.fuel.2026.138969
Received 30 October 2025; Received in revised form 21 January 2026; Accepted 28 February 2026
Available online 6 March 2026

(i) heating by convection and radiation
(ii) drying of inherent moisture
(iii) devolatilisation of embedded light gases
(iv) homogeneous combustion of the light gases
(v) heterogeneous conversion of the remaining char

These processes typically proceed in sequence, but overlaps may arise and must be accurately captured in modelling.

Previous experimental investigations [2–7] have shown that processes (iii), (iv) and (v) can significantly overlap, depending on the particle properties such as coal type and particle size, and the operating conditions in the furnace, e.g. ambient gas conditions and temperature. These studies were able to experimentally identify the transition between these processes through the observed ignition modes, namely *homogeneous*, *heterogeneous* or *hetero-homogeneous* ignition. Homogeneous and heterogeneous ignition modes correspond to the isolated processes (iv) and (v), respectively, whereas hetero-homogeneous ignition is associated with the simultaneous occurrence of processes (iv) and (v). It is also worth noting that process (iv) is a consequence of process (iii). From a modelling point of view, the overlap has a great importance. Various modelling approaches [5–9] have been employed to quantify the hetero-homogeneous ignition mode under various conditions, typically based on reduced-order devolatilisation and char conversion models.

Rather than following the classical approach of quantifying the overlap between processes (iv) and (v), the present study attempts to assess the potential overlap of processes (iii, devolatilisation) and (v, char conversion), while process (iv, homogeneous combustion) may proceed simultaneously. Moreover, in large-scale simulations of solid fuel particles, Euler–Lagrange approaches are typically employed together with simplified devolatilisation and char conversion sub-models [10–19]. In such studies, and in the context of modelling strategies, it is commonly assumed that processes (iii) and (v) occur sequentially or with a small, user-defined overlap, e.g. char conversion starts once a specified fraction of volatiles has been released. This study is further motivated by a limitation of modelling approaches for solid fuel conversion in the Euler-Lagrange context, such as flamelets [20–30], Multiple Mapping Conditioning (MMC) [31] and others. While e.g. flamelet models can potentially account for overlapping processes (iii), (iv) and (v) they—when applied in the Euler-Lagrange context—do *not* account for overlapping effects that occur directly in the boundary layer near the particle surface. For instance, displacement of oxygen from the particle surface during the devolatilisation process (iii) can delay char conversion, because less O_2 is available for process (v). Neglecting this interference induces errors in the particle near-field and affects the overall burning behaviour.

To accurately quantify the overlap between processes (iii), (v) [and partially also (iv)] we investigate the conversion of single coal particles using a detailed boundary layer resolved simulation (BLRS) approach. In BLRS, the computational grid resolves all relevant gradients and the gas-solid exchange is represented through a set of boundary conditions. Although this approach offers high accuracy, its significant computational cost restricts its application to single particles [32–36] and small particle groups [37–39]. However, previous BLRS studies have demonstrated that this modelling approach is well-suited for improving our understanding of particle conversion processes and supporting model development [32,34,36].

In the present study, the conversion of single coal particles is investigated using BLRS for various ambient conditions and particle sizes. The gas phase is described with detailed homogeneous kinetics [33]. The solid phase is defined as a porous medium and described using a detailed, yet flexible multi-step kinetic approach for (iii) devolatilisation [40] and (v) char conversion [41] to examine the overlap of these two processes. To the best of our knowledge, no numerical studies have yet investigated the overlap between devolatilisation and char conversion with such high model fidelity in BLRS. The objectives of the present study are to

- propose a methodology and criteria for assessing the overlap of devolatilisation and char conversion,
- evaluate the overlap of devolatilisation and char conversion for varying ambient conditions and particle sizes,
- develop a regression to integrate the extent of overlap into simplified sub-models.

The remainder of this paper is organised as follows: Section 2 outlines the BLRS approach, followed by a description of the computational setup in Section 3. Results are presented and discussed in Section 4 and the main conclusions are given in Section 5.

2. Modelling

As in our previous study by Tufano et al. [33], the modelling strategy adopted in the present work differentiates between the particle interior and exterior, with the two regions separated by a spherical interface. The mathematical description for both regions is presented in the following.

2.1. Particle exterior

The particle exterior is treated as a reacting continuum and is described by the governing equations for total mass, momentum, energy and chemical species as

$$\frac{\partial \rho}{\partial t} + \frac{\partial}{\partial x_i}(\rho u_i) = 0, \tag{1}$$

$$\frac{\partial}{\partial t}(\rho u_i) + \frac{\partial}{\partial x_j}(\rho u_i u_j) = -\frac{\partial p}{\partial x_i} + \frac{\partial}{\partial x_j}\left(\mu\left[\frac{\partial u_j}{\partial x_i} + \frac{\partial u_i}{\partial x_j} - \frac{2}{3}\frac{\partial u_m}{\partial x_m}\delta_{ij}\right]\right), \tag{2}$$

$$\frac{\partial}{\partial t}(\rho T) + \frac{\partial}{\partial x_i}(\rho u_i T) = \frac{\partial}{\partial x_i}\left(\frac{\lambda}{c_\mathrm{p}}\frac{\partial T}{\partial x_i}\right) - \rho\frac{c_{\mathrm{p},k}}{c_\mathrm{p}}Y_k V_{c,i} + \dot{S}_{T,\mathrm{rad}} + \dot{\omega}_{T,\mathrm{chem}}, \tag{3}$$

$$\frac{\partial}{\partial t}(\rho Y_k) + \frac{\partial}{\partial x_i}(\rho u_i Y_k) = \frac{\partial}{\partial x_i}\left(\rho D_k \frac{\partial Y_k}{\partial x_i}\right) - \frac{\partial}{\partial x_i}(\rho V_{c,i} Y_k) + \dot{\omega}_{k,\mathrm{chem}}\,. \tag{4}$$

Here, subscripts $<i,j>$ indicating the coordinate directions, x the spatial coordinate, t the time, ρ the density, u the velocity, T the temperature, λ the heat conductivity, c_p the specific heat capacity and $\dot{S}_{T,\mathrm{rad}}$ the radiative source term. Y_k is the mass fraction of chemical species k, D_k is the mass diffusivity, $\dot{\omega}_{T,\mathrm{chem}}$ and $\dot{\omega}_{k,\mathrm{chem}}$ the heat release and species reaction rates from homogeneous chemical reactions, respectively. Radiative heat transfer is considered by the P1 model and differential species diffusion is modelled by a mixture-averaged approach [42]. $V_{c,i}$ is a corrective diffusion velocity vector to enforce mass conservation and is employed as [42,43]

$$V_{c,i} = D_k \frac{\partial Y_k}{\partial x_i}. \tag{5}$$

2.2. Particle interior

The particle interior is treated as a porous medium and is divided into a gas phase (subscript $<g>$) and solid phase (subscript $<s>$). The two sub-volumes of each phase are determined as

$$V_g = V_p \cdot \epsilon \qquad \text{and} \qquad V_s = V_p \cdot (1-\epsilon), \tag{6}$$

with V_p denoting the total particle volume and ϵ the particle porosity. Because of these two distinct phases, separate sets of conservation equations must be solved for each:

- Solid phase:

The conservation of total mass and chemical species are calculated as [33,44]

$$\frac{\partial}{\partial t}(\rho_s(1-\epsilon)) = \sum_{k=1}^{N_s} \dot{\omega}_{k,s}, \tag{7}$$

$$\frac{\partial}{\partial t}(\rho_s Y_{k,s}(1-\epsilon)) = \dot{\omega}_{k,s}, \tag{8}$$

with N_s the number of solid species and $\dot{\omega}_{k,s}$ the solid species reaction rates.

- Gas phase:

For the gas phase, the conservation equations of total mass, momentum and chemical species are solved as

$$\frac{\partial}{\partial t}(\rho_g \epsilon) + \frac{\partial}{\partial x_i}(\rho_g u_i) = \sum_{k=1}^{N_g} \dot{\omega}_{k,g} \tag{9}$$

$$\frac{\partial}{\partial t}(\rho_g u_i \epsilon) + \frac{\partial}{\partial x_j}(\rho_g u_i u_j) = -\frac{\partial p}{\partial x_i} + \frac{\partial}{\partial x_j}\left(\mu_g\left[\frac{\partial u_j}{\partial x_i} + \frac{\partial u_i}{\partial x_j} - \frac{2}{3}\frac{\partial u_m}{\partial x_m}\delta_{ij}\right]\right) + \mathbf{S} \tag{10}$$

$$\frac{\partial}{\partial t}(\rho_g Y_{k,g}\epsilon) + \frac{\partial}{\partial x_i}(\rho_g u_i Y_{k,g}) = \frac{\partial}{\partial x_i}\left(\rho D_{k,g}\frac{\partial Y_{k,g}}{\partial x_i}\right) - \frac{\partial}{\partial x_i}\left(\rho_g V_{c,i} Y_{k,g}\right) + \dot{\omega}_{k,g} \tag{11}$$

where N_g represents the number of gaseous species, $\dot{\omega}_{k,g}$ the reaction rates of the gaseous species obtained form the heterogeneous reaction mechanism and $\mathbf{S}$ the momentum source term for the porous media as defined by the Darcy-Forchheimer law [33].

- Energy conservation in the particle interior:

Finally, energy conservation in the particle interior is considered through the processes of conduction, convection and chemical reaction. Assuming local thermal equilibrium, the joint energy equation for both phases is formulated as follows

$$c_{p,g}\frac{\partial}{\partial t}(\rho_g T_p \epsilon) + c_{p,g}\frac{\partial}{\partial x_i}(\rho_g u_i T_p) + c_{p,s}\frac{\partial}{\partial t}(\rho_s T_p(1-\epsilon)) = \frac{\partial}{\partial x_i}(\lambda_{\text{eff.}}\frac{\partial T_p}{\partial x_i}) + \dot{Q}_{\text{chem}} \tag{12}$$

with T_p the internal particle temperature, $\lambda_{\text{eff.}}$ the effective thermal conductivity [33] and $\dot{Q}_{\text{chem}}$ the heat release by chemical reactions. The remaining coefficients of the porous media model and additional details are provided in [33,44].

2.3. Interface particle interior/exterior

In the BLRS approach, the coupling between the particle interior (subscript <int.>) and exterior (subscript <ext.>) is realised through a set of boundary conditions at the particle surface. The boundary conditions are given as

- Pressure

$$p_{\text{int.}} = p_{\text{ext.}} = 103125\,\text{Pa} \tag{13}$$

- Velocity

$$\left.\frac{\partial u_i}{\partial x_i}\right|_{\text{int.}} = 0 \tag{14}$$

- Solid phase species

$$\frac{\partial Y_{k,s}}{\partial x_i} = 0 \tag{15}$$

- Gas phase species

$$\rho_g D_{\text{eff.},k}\left.\frac{\partial Y_{k,g}}{\partial r}\right|_{\text{int.}} = \rho D_k \left.\frac{\partial Y_k}{\partial r}\right|_{\text{ext.}} \tag{16}$$

- Temperature

$$\lambda_{\text{eff.}}\left.\frac{\partial T_p}{\partial r}\right|_{\text{int.}} = \lambda\left.\frac{\partial T}{\partial r}\right|_{\text{ext.}} + S_{\text{rad}} \tag{17}$$

where the surface radiative heat flux S_{rad} is determined using the Marshak boundary condition with particle absorption coefficient $\epsilon_p = 1.0$ [33] and $D_{\text{eff.},k}$ the effective pore diffusion coefficient [33,41]

$$D_{\text{eff.},k} = \left[\frac{1}{D_k^m} + \frac{1}{D_k^{\text{Kn}}}\right]^{-1} \cdot \frac{\epsilon}{\tau^2} \tag{18}$$

where D_k^m is the molecular diffusivity, τ tortuosity and D_k^{Kn} the Knudsen diffusivity calculated as

$$D_k^{\text{Kn}} = \frac{d_{\text{por}}}{3}\sqrt{\frac{8}{\pi}\frac{RT}{M_k}} \tag{19}$$

with particle pore diameter $d_{\text{por}} = 0.3\,\mu\text{m}$ [41], universal gas constant R and molar mass M_k of species k.

2.4. Kinetic models

2.4.1. Homogeneous gas phase reactions

The kinetics used for homogeneous gas phase reactions are based on a skeletal mechanism derived from a reduction of the detailed CRECK-G-1407 model [33]. This mechanism comprises 76 species and 973 reactions, describing both the devolatilisation and oxidation of light and heavy hydrocarbon species.

2.4.2. Heterogeneous reactions

In this work, a detailed multi-step heterogeneous kinetic model (CRECK-S-C) [45] for coal devolatilisation [40] and char conversion [41] is employed. The model consists of a total of 40 species and 49 reactions. The devolatilisation process is described by 32 species and 35 reactions, while 8 species and 14 reactions represent char oxidation, char annealing and char gasification. The volatile matter released during pyrolysis consists of a complex mixture of light gases and heavy tars, with the latter being modelled as lumped species (see Table 1).

2.5. Coal properties

In the present study, Pittsburgh seam high-volatile bituminous coal [46] is selected as the fuel, with its proximate and ultimate analyses given in Table 2. Rather than describing the coal directly by its ultimate and proximate analyses, the latter are used to represent it in terms of three reference coals derived through linear interpolation, which are then employed in the detailed multi-step kinetic model. The composition in terms of the reference coals in mass-% is COAL1 = 27.90, COAL2 = 49.41, COAL3 = 12.69 and Ash = 10 [33]. The fixed carbon in the prox-

Table 1
Lumped species of heavy tars in mass-% [33].

TAR1	$25.8C_{10}H_{12} + 74.2C_{12}H_8$
TAR2	$22.4C_{10}H_7CH_3 + 50.8C_{20}H_{10} + 26.8C_{11}H_{12}O_4$
TAR3	$9.7C_{10}H_7CH_3 + 22.1C_{20}H_{10} + 27.3C_9H_{10}O_2 + 40.8C_{11}H_{12}O_4$
BTX2	$41.8C_{10}H_7CH_3 + 58.2C_{10}H_{12}$

Table 2
Properties of Pittsburgh seam high-volatile bituminous coal [46].

Ultimate analysis (wt% daf)		Proximate analysis (wt% dry)	
C	75.23	Fixed carbon	37.9
H	5.16	Volatile matter	35.89
O	9.83	Moisture	0.47
N	1.43	Ash	6.95
S	2.00		
HHV [MJ/kg]	30.94		

imate analysis Table 2 is initially contained within COAL1, COAL2 and COAL3. During the conversion of the reference coals, this bound fixed carbon is transformed into reactive CHAR. The coal used in the present study follows [33,46]. It has a density of $\rho_s = 1400\,\mathrm{kg/m^3}$, heat capacity of $c_{\mathrm{p},s} = 1680\,\mathrm{J/(kg\,K)}$, thermal conductivity of $\lambda_s = 0.3\,\mathrm{W/(m\,K)}$, initial porosity of $\epsilon_0 = 0.25$ and an initial tortuosity of $\tau_0 = \sqrt{2}$.

2.6. Model validation

The detailed multi-step heterogeneous kinetic model of Maffei [45] and co-workers has been adopted in this work to jointly predict coal devolatilisation [40], char conversion [41] and homogeneous volatile combustion [33]. The kinetic sub-model for coal devolatilisation has been extensively validated in previous studies against a wide range of experimental datasets, covering various reactors, coal types (including Pittsburgh high-volatile bituminous coal), heating rates and initial particle temperatures [40]. The char conversion sub-model has similarly been validated using drop-tube reactor experiments for two coal types, namely Pittsburgh high-volatile bituminous coal and Beulah lignite, under quiescent gas conditions and varying environmental compositions [41]. The model has further been extended to include homogeneous gas phase reactions in [33], where a good agreement with experimental measurements was achieved. Collectively, these prior validation studies demonstrate that the applied sub-models, especially the kinetics, are well-suited to assess the overlap between devolatilisation, char conversion and homogeneous volatile combustion for the present work.

3. Computational configuration

3.1. Computational setup

The computational domain used in this study follows the configuration from our previous work [47] and is schematically illustrated in Fig. 1. It is a two-dimensional wedge with a 5 degree angle. The domain extends $L_x = 100 \cdot d_p$ in the streamwise direction and $L_y = 33.5 \cdot d_p$ in the crosswise direction. The domain is large enough to avoid boundary effects. The coal particle is positioned at the origin of the coordinate system ($x = y = 0$) with an upstream region length of $33 \cdot d_p$ and a downstream region length of $66 \cdot d_p$. The particle interior is discretised into 30 cells in the radial and 72 cells in the circumferential direction, which results in a cell size of approx. $0.02 \cdot d_p$ within both the particle interior and the surrounding boundary layer. The smallest cells are located at the particle surface to resolve the particle boundary layer. The cell size increases progressively with distance from the particle. The mesh is fixed and remains unchanged throughout the simulations. We conducted a mesh independence study by considering four mesh resolutions ($0.03 \cdot d_p, 0.02 \cdot d_p, 0.015 \cdot d_p, 0.01 \cdot d_p$) for four particle diameters ($d_p = 25, 50, 100, 150\,\mu\mathrm{m}$) at $T = 1400\,\mathrm{K}$ and $X_{\mathrm{O_2}} = 0.21$. We found that the relative error in the peak gas temperature is below 5%, while the relative error in the flame stand-off distance is below 10% when the smallest mesh size is coarsened from $0.01 \cdot d_p$ to $0.02 \cdot d_p$. Conversely, refining the mesh from $0.02 \cdot d_p$ to $0.01 \cdot d_p$ increases the computational cost by up to 213%.

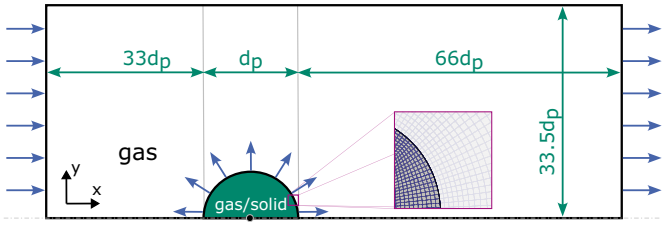

Fig. 1. Schematic illustration (not to scale) of the computational domain.

A laminar flow at atmospheric pressure, constant temperature and constant composition (O_2-N_2) enters the domain from the left, with the same values applied as initial fields in the domain interior. The inlet velocity is set to a small value of $5 \cdot 10^{-4}\,\mathrm{m/s}$ to mimic quiescent flow conditions. The initial temperature of the solid particle is set to 600 K, to reduce the computational cost associated with the early stage of particle heating. In our preliminary studies, we found that reactions occurring during particle heating between 300–600 K were negligible. Therefore we omitted this initial heat-up phase from the present analysis.

A total of 45 simulations is conducted by varying three key parameters, namely the surrounding gas temperature (1000 K, 1400 K and 1800 K), particle diameter (25 μm, 50 μm, 100 μm, 125 μm and 150 μm) and oxygen concentration (5%, 21% and 70%). Cases with high oxygen concentrations are included, as such conditions are typical for oxyfuel combustion conditions. These parameters have been identified in the literature as the most influential factors affecting coal particle conversion [46,48,49]. It is also worth noting that increasing the inlet velocity and thus the particle Reynolds number, can significantly influence heat and mass transfer for particles larger than 100 μm [39]. However, these effects are ignored here due to the assumption of quiescent gas conditions.

The simulations are performed using a validated finite volume solver [33] based on OpenFOAM-v2012. The solver is coupled with the OpenSMOKE++ library [50] to solve both the multi-step heterogeneous kinetics and homogeneous gas phase chemistry simultaneously.

3.2. Methodology and criterion for assessing process overlap

3.2.1. Methodology to identify process overlap

The methodology to identify the overlap of the devolatilisation and char conversion processes is based on the rate of production analysis (ROPA) of the multi-step heterogeneous kinetics of the solid fuel particle. The total devolatilisation rate is defined as the sum of the production rates of all volatile species resulting from reactions classified as devolatilisation reactions in the multi-step solid kinetics. In the present study, the numbering convention of the solid phase kinetics presented in the *supplementary data 2* of [33] is adopted. Therefore, a total of 34 reactions (reactions #1 to #33 and #38) are considered to characterise devolatilisation

$$\dot{m}_{\mathrm{dev}} = \sum_R \sum_k \dot{\omega}_{k,R} M_k \quad \text{with} \quad \begin{matrix} R = \#1\text{-}\#33, \#38 \\ k = k_{\mathrm{dev}} \end{matrix} \tag{20}$$

with k_{dev} indicating the devolatilisation species. The overall char conversion process comprises of char annealing (reactions #34 to #36), char oxidation (reactions #39 to #43) and char gasification (reaction #44 to #49). Simplified char conversion sub-models in the Euler-Lagrange framework typically consider only the oxidation of C with oxygen to CO or CO_2. Accordingly, in the following discussion the term *char conversion* is defined in terms of the 5 reactions of char species (k_{char}) oxidation, as shown in Table 3 and is calculated as

$$\dot{m}_{\mathrm{char}} = \sum_R \sum_k \dot{\omega}_{k,R} M_k \quad \text{with} \quad \begin{matrix} R = \#39\text{-}\#43 \\ k = k_{\mathrm{char}} \end{matrix} \tag{21}$$

with M_k the molecular weight of species k.

Table 3
Char oxidation reactions.

Nr.	Reaction equation
#39	$CHARH + 0.75O_2 \rightarrow 0.5H_2O + CO + CHAR$
#40	$CHAR + O_2 \rightarrow CO_2$
#41	$CHAR + 0.5O_2 \rightarrow CO$
#42	$CHARG + O_2 \rightarrow CO_2$
#43	$CHARG + 0.5O_2 \rightarrow CO$

3.2.2. Criterion to quantify process overlap

The overlap period is defined as the time when the two processes of devolatilisation and char conversion occur simultaneously without a significant difference (defined as one order of magnitude) between their mass conversion rates as

$$\text{overlap} : 0.1 \leq \frac{\dot{m}_{\text{dev}}}{\dot{m}_{\text{char}}} \leq 10 \tag{22}$$

with $\dot{m}_{\text{dev}}$ and $\dot{m}_{\text{char}}$ the sum of production mass rates of all volatile species (Eq. 20) and char oxidation species (Eq. 21), respectively. Once the overlap period is identified, it is more advantageous to establish a physics-based criterion for initiating the char conversion sub-model [29,51,52]. A helpful definition would be to know the start of the overlap after a certain fraction of the available volatile mass has been released. This approach is well established and commonly applied in reduced-order models to activate an explicit char conversion sub-model. Characterising the start of the overlap as time t_s and the total time required for complete volatile gas release with t_{dev}, the fraction of volatile mass released at the start of the overlap is given as

$$Y_{\text{OL}} = \frac{m_{\text{dev}}(t_s)}{m_{\text{dev}}(t_{\text{dev}})} = \frac{\int_0^{t_s} \dot{m}_{\text{dev}}(t)}{\int_0^{t_{\text{dev}}} \dot{m}_{\text{dev}}(t)} \tag{23}$$

with

$$t_s = \min\left\{ t > 0 : 0.1 \leq \frac{\dot{m}_{\text{dev}}}{\dot{m}_{\text{char}}} \leq 10 \right\}. \tag{24}$$

The definition in Eq. (23) will be used in the following to quantify the overlap under various conditions.

4. Results and discussion

4.1. Particle conversion and homogeneous reactions (reference case)

This section discusses the particle conversion process with homogeneous gas phase ignition and combustion for a reference case with $d_p = 50\,\mu\text{m}$, $X_{O_2} = 0.21$ and $T = 1400\,\text{K}$. Fig. 2 shows the evolution of the maximum gas phase temperature $\max(T_g)$, along with the volume-averaged temporal profiles of the particle temperature T_p and selected species inside the particle. For convenience and ease of comparison with later plots, the mass percentage of O_2 is plotted twice in Fig. 2, once in olive to directly compare its evolution with T_p and $\max(T_g)$ at the top, and once again in blue at the bottom, to directly compare it with the light volatile gases and TAR. Fig. 3 illustrates the corresponding gas phase OH mass fraction and gas temperature fields in the vicinity of the coal particle.

At the initial stage, the colder coal particle is introduced into a hot environment, see red vs. light blue line in Fig. 2 (top) at $t = 0$. At this time, the particle consists only of reference coals COAL1 (hydrogen-rich, black line), COAL2 (bituminous, dark-red line) and COAL3 (lignitic, purple line), as shown in Fig. 2 (centre). The particle composition remains unchanged until $t = 1\,\text{ms}$, as the particle temperature in Fig. 2 (top) is not yet sufficiently high to initiate the conversion processes. Up to 1 ms, the particle temperature rises sufficiently high to start the formation of TAR compounds (green), see Fig. 2 (bottom), indicating the first stage of the devolatilisation process. From $t = 1.75$ to $2.45\,\text{ms}$, COAL2 and COAL3 are quickly consumed, while the fraction of COAL1 and (reactive) CHAR

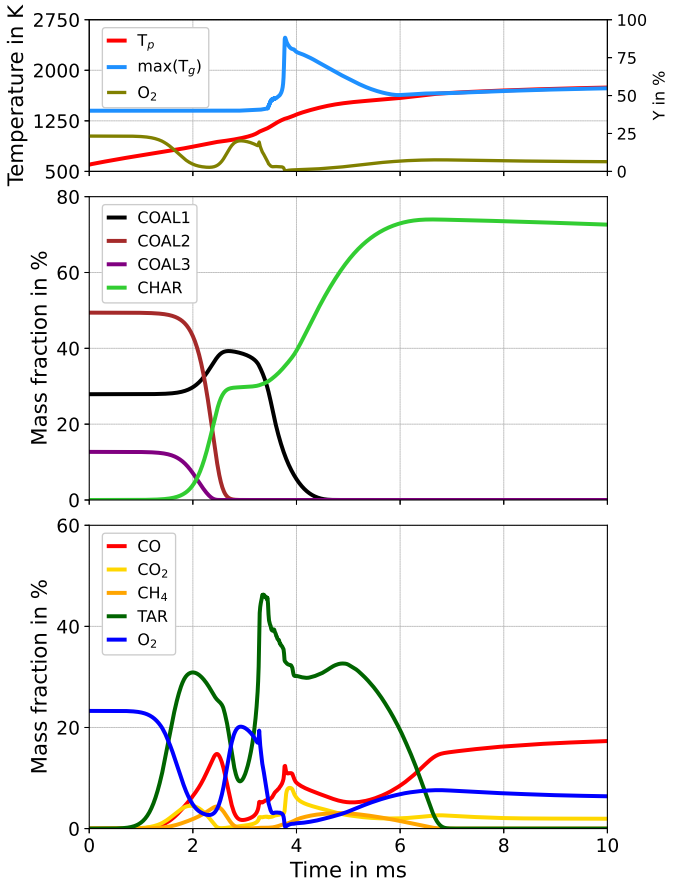

Fig. 2. Temporal evolution of maximum gas phase temperature, volume-averaged particle temperature and volume-averaged mass fractions in the interior of the particle for the reference case. Top: Averaged particle temperature, maximum gas temperature and O_2 mass percentage. Centre: Reference coals and CHAR. Bottom: Volatile species CO, CO_2, O_2, CH_4 and TAR. CO, CO_2, O_2 and CH_4 represents the light gases and TAR the sum of all species in Table 1. (For interpretation of the references to colour in this figure legend, the reader is referred to the web version of this article.)

increases. CHAR is referred to as a sum of CHAR, CHARH and CHARG. Simultaneously, the light volatile species CO (red), CO_2 (yellow), CH_4 (orange) and more TAR are produced within the particle through the conversion of COAL2 and COAL3, as shown in Fig. 2 (bottom). The accumulation of these volatiles displaces O_2 from the particle interior. As the process continues, the formation of volatiles in the particle interior proceeds. These gaseous volatiles then follow Eqs. (8) to (11) inside the particle, eventually leading to their release to the particle exterior. This release is visualised by the outward-pointing velocity vectors at the particle surface at $t = 2.45\,\text{ms}$ in Fig. 3. However, at this stage the amount of released volatiles and their mixing with the surrounding air is still insufficient to initiate homogeneous gas phase ignition and volatile combustion, as indicated by the near-zero OH concentration (dark-blue) and the unchanged background gas temperature (black).

At $t = 3\,\text{ms}$, COAL2 and COAL3 have been completely consumed, as shown in Fig. 2 (centre), indicating that the first stage of devolatilisation has been completed. At this time, COAL1 reaches its maximum concentration, while the CHAR fraction shows a plateau. This completion is further confirmed in Fig. 2 (bottom), where all volatile species show a local minimum in their concentration profiles. Due to the decrease in volatile production, O_2 from the surrounding environment starts to re-enter the particle. However, the internal O_2 concentration does not surpass 20 mass-% due to the continued, moderate release of TAR and CO from the remaining COAL1. The disappearance of outward-pointing velocity vectors at the particle surface in Fig. 3 at $t = 3\,\text{ms}$ further

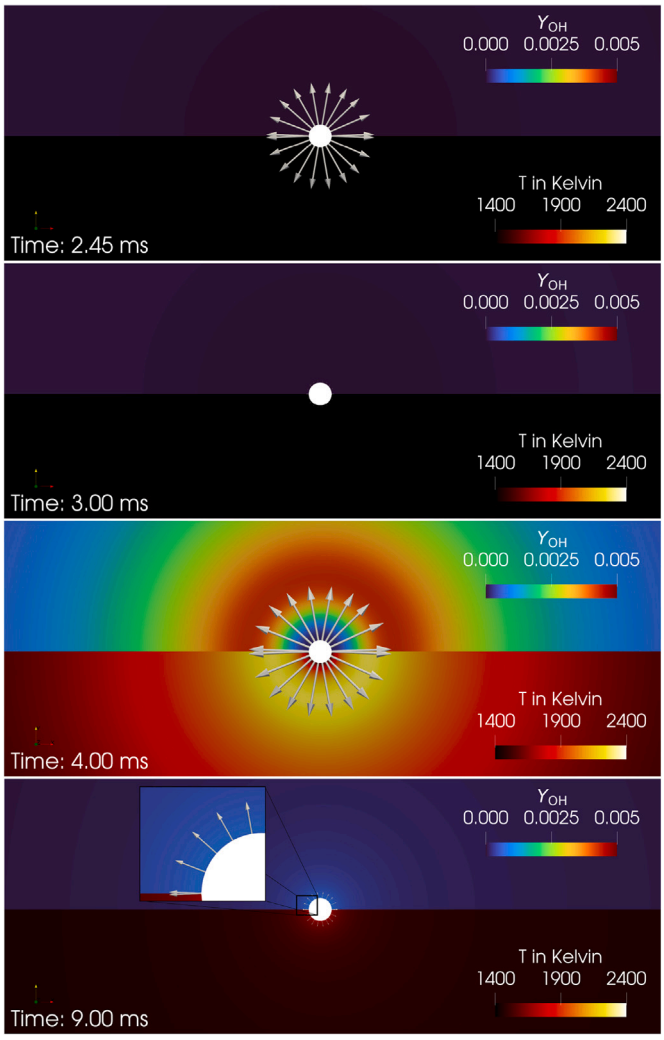

Fig. 3. Snapshots of the OH mass fraction (top half) and gas temperature field (lower half) in the vicinity of the coal particle surface at selected times for the case with $d_p = 50\,\mu m$, $X_{O_2} = 0.21$ and $T = 1400\,K$. Velocity vectors at the particle surface are scaled by their magnitude. (For interpretation of the references to colour in this figure legend, the reader is referred to the web version of this article.)

confirms the end of the first devolatilisation stage. However, the volatiles released during this stage do not immediately initiate homogeneous gas phase ignition and combustion, as shown in Fig. 2 (top, light-blue) since some time is required for mixing and reaching the lower flammability limit with the surrounding oxygen. The maximum gas phase temperature reveals a two-stage ignition process. The first ignition stage is characterised by a small temperature rise associated with low temperature reactions, followed by a second stage marked by a steeper temperature increase, during which high-temperature chemical pathways become dominant.

From $t = 3$ ms onwards, the second stage of devolatilisation begins, as indicated by the consumption of COAL1 and the further formation of CHAR in Fig. 2 (centre). This stage is characterised by the repeated release of light volatile species and substantial amounts of TAR, together with the displacement and consumption of O_2 within the particle, as can be observed in Fig. 2 (bottom). The second devolatilisation stage continues until approximately $t = 7$ ms, as indicated by the decrease of TAR to zero at this point. Notably, at $t = 4$ ms, the profile of TAR shows a local minimum before rising again. The reason for this behaviour can be explained by Fig. 3 at $t = 4$ ms. In the previous time period between $t = 3$ and 4 ms, a sufficient volatile mass has been released into the environment and mixed with O_2, which leads to the start of homogeneous gas phase ignition and combustion, indicated by the sharp increase in maximum gas phase temperature in Fig. 2 (top). Now at $t = 4$ ms, outward-pointing velocity vectors at the particle surface indicate the continued release of volatiles. A high OH concentration (red region) can be identified, surrounding the particle and indicating the presence of a highly reactive zone. The corresponding temperature field shows a significant increase in gas phase temperature (yellow–white regions) within this zone, confirming the development of a flame enveloping the particle. Heat released from the flame between $t = 3.5$ and 6 ms in Fig. 2 (top) accelerates particle heating and promotes further volatile release, as reflected by the increase in TAR after $t = 4$ ms in Fig. 2 (centre). Conversely, the homogeneous gas phase reactions also lead to oxygen consumption in the vicinity of the particle, reducing its availability for the char conversion process, as shown by the oxygen profiles dropping to nearly zero at $t = 3.9$ ms in Fig. 2 (bottom). Additionally, between $t = 3$ and 3.5 ms, the particle temperature profile in Fig. 2 (top) shows a steeper slope, in the absence of heat released from the flame. This behaviour can be attributed to the heat generated by char conversion. During this period, both oxygen and (reactive) CHAR are present within the particle, leading to char conversion, as evidenced by the decrease in oxygen and the corresponding increase in CO and CO_2 shown in Fig. 2 (bottom).

Between $t = 5$ and 7 ms, the solid composition of the particle consists mainly of CHAR, as shown in Fig. 2 (centre). During this period, no additional volatiles are produced in the particle interior, but instead, the present volatile species within the particle are gradually released into the gas phase, as indicated by the decline in CH_4 and TAR profiles in Fig. 2 (bottom). At the same time, some heavy TAR compounds decompose into smaller species, as observed by the increase in CO and CO_2 concentrations. The overall decrease in volatile content is further evidenced by the rise in the O_2 profile within the particle.

From $t = 7$ ms onwards, a slight decrease in CHAR and O_2 and simultaneously a gradual increase in particle temperature, CO and CO_2 can be observed in Fig. 2. The concurrent evolution of these species indicates that the char conversion process is proceeding at this stage. In Fig. 3 at $t = 9$ ms, both the OH concentration and gas phase temperature decrease toward near-zero and ambient levels, respectively, showing the absence of volatile species and flame extinction in the gas phase. However, small outward-pointing velocity vectors remain visible around the particle, indicating the continued release of gaseous products, i.e., CO and CO_2, from char conversion. A slightly elevated gas temperature in the vicinity of the particle further confirms this observation, which is due to the heat release by char oxidation and the subsequent heat transfer to the surrounding gas phase. The char conversion process continues until all remaining carbon is fully oxidised (CHAR $\rightarrow 0$ for $t \rightarrow \infty$ in Fig. 2 (centre)), leaving only the residual ash particle (not shown). However, this process takes too long for the present BLRS approach such that the end of char conversion cannot be computed.

Overall, Figs. 2 and 3 show that the particle undergoes devolatilisation and char conversion during the overall conversion process. However, these plots do not clearly indicate any exact ending of devolatilisation or start of the char conversion phase. Since (reactive) CHAR formation within the particle begins at approximately $t = 1.5$ ms, it is possible that char conversion can start from this time. For a better quantification of the start of the char conversion process and potential overlap with devolatilisation, we applied the methodology presented in Section 3.2, resulting in Fig. 4. The third devolatilisation stage is associated with metaplast reactions as will be discussed next.

Fig. 4 illustrates the total devolatilisation rate (blue) and char conversion rate (orange) as a function of time for the reference case. The vertical dashed line at $t = 3$ ms indicates the end of the first and the beginning of the second stage of devolatilisation, while the line at $t = 7$ ms denotes the end of the second and the start of the third stage of

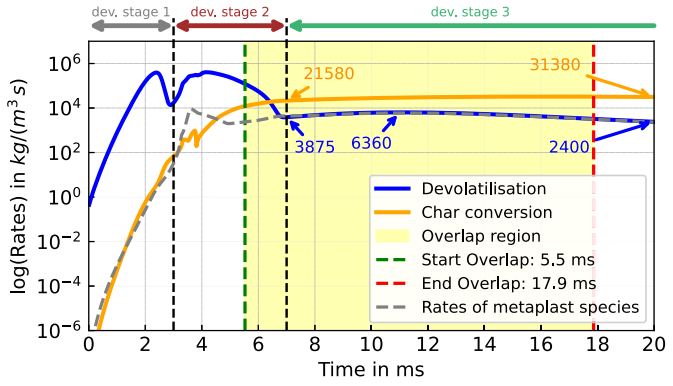

Fig. 4. Temporal evolution of the total devolatilisation rate (blue, solid line), char conversion rate (orange, solid line) and total rates of metaplast species (grey, dashed line) for the reference case. The vertical dashed lines indicate the start (green) and end (red) of overlap. The grey, brown and light-blue arrows indicate the time period of first, second and third stage of devolatilisation, respectively. (For interpretation of the references to colour in this figure legend, the reader is referred to the web version of this article.)

devolatilisation. Devolatilisation begins with a low rate at $t = 0$ ms and rises to a local maximum rate at $t = 2.45$ ms, marking the first stage of devolatilisation (grey arrow). After this stage is completed, the rate decreases to a local minimum at $t = 3$ ms, before rising again to another local maximum at $t = 4$ ms, indicating the start of the second devolatilisation stage (brown arrow). The second stage concludes at approximately $t = 7$ ms at a value of 3875 kg/(m^3 s), until which the rate significantly decreases. For $t > 7$ ms, the devolatilisation rate gradually increases to a local maximum at $t = 11$ ms with a value of 6360 kg/(m^3 s) before slowly decreasing to a value of 2400 kg/(m^3 s) as $t \to 20$ ms. The slight increase after the second devolatilisation stage is caused by the slow conversion of metaplast species (CH_4^*, CH_2^*, CO_2^*, HO_2^*, H_2^* and CO^*) involved in reactions #25-#33. The total rate of the metaplast conversion reactions is shown in Fig. 4 (grey, dashed line) and illustrates that during the third devolatilisation stage, for $t > 7$ ms the devolatilisation rate is solely composed of the metaplast reactions. Based on this observation, the third stage of devolatilisation (light-blue arrow) is consistently associated with the dominance of metaplast reactions in the following analysis.

The char conversion rate at $t = 0$ ms starts at zero (not shown), due to the absence of (reactive) CHAR at the initial stage. As time progresses, more CHAR is produced (see Fig. 2 (centre)) that can react with O_2 in the particle interior, leading to a gradual increase in the char conversion rate. Between $t = 3$ and 4 ms, small wiggles in the char conversion rate can be observed. This behaviour has two contributing factors. Firstly, it results from the transition between the first and second devolatilisation stages, during which O_2 re-enters the particle (see Fig. 2 (bottom)). With both (reactive) CHAR and O_2 present within the particle, the char conversion rate rises. However, the release of volatiles during the second devolatilisation stage displaces O_2, causing the observed wiggles. Secondly, as previously noted for Figs. 2 and 3, the profile of char conversion rate is further influenced by oxygen consumption from homogeneous gas phase reactions, which reduces the oxygen available for char conversion.

By applying the criterion for quantifying the overlap between devolatilisation and char conversion, as presented in Section 3.2.2, using Eq. (22), the overlap region of the reference case is identified to start at $t = 5.5$ ms and to end at $t = 17.9$ ms. During this interval, both processes occur simultaneously and are of the same order of magnitude. Additionally, Eq. (23) yields the fraction of volatile mass released at the start of the overlap for the reference case as

$$Y_{\mathrm{OL,ref}} = 83.49\% .$$

The value indicates that char conversion process starts once 83.49% of the initially contained volatiles has been released. The limits applied in reduced-order models [29,51,52] are in agreement with our findings.

To quantify the error introduced by neglecting the overlap between devolatilisation and char conversion, we compared the devolatilisation release rates for different particle diameters at $T = 1400$ K and $X_{O_2} = 0.21$. Neglecting the overlap by switching off char conversion delays the third stage for small particles ($d_p < 100$ µm), but can shift it to earlier times for larger particles ($d_p \geq 100$ µm), which contain more volatiles and allow continuous volatile release, enhanced gas phase reactions and further promotion of devolatilisation (see also Section 4.4). We quantified the error by evaluating the shift of the end of the second stage devolatilisation, which amounts to approx. +15% for $d_p = 25$ µm and −5% for $d_p = 150$ µm.

Further analyses of the variation in the oxygen concentration, ambient temperature and particle diameter are presented in the following subsections.

4.2. Variation of oxygen concentration

Fig. 5 shows the same quantities as before in Figs. 2 and 4 (top) for different oxygen concentrations, i.e. $X_{O_2} = \{0.05, 0.70\}$, at a particle diameter of $d_p = 50$ µm and an ambient temperature of $T = 1400$ K.

A consistent trend can be observed by comparing Fig. 4 ($X_{O_2} = 0.21$) and Fig. 5. With increasing oxygen concentration, the beginning of the

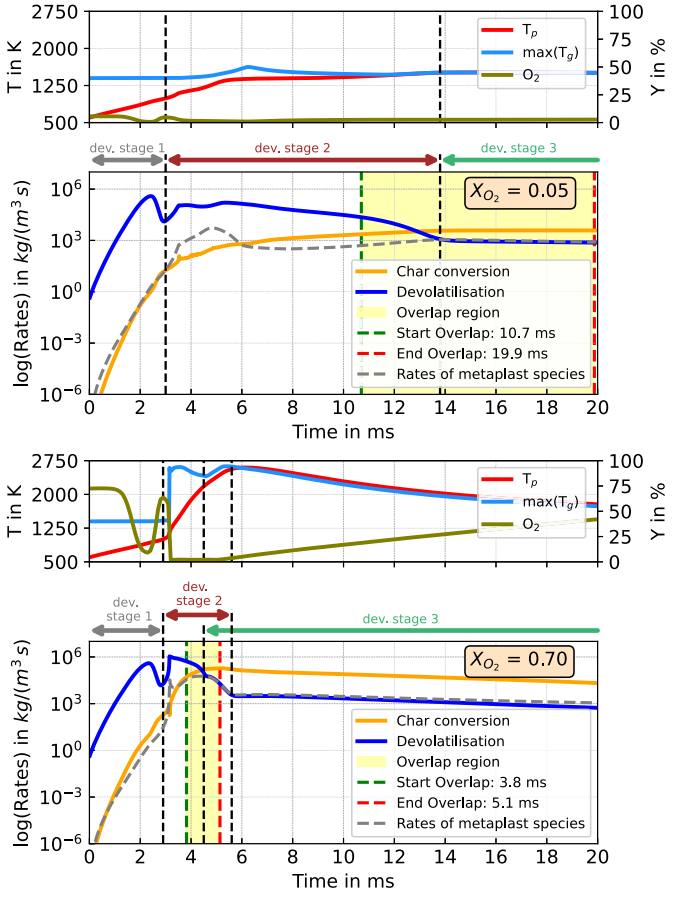

Fig. 5. Temporal evolution of the maximum gas phase temperature (light-blue), volume-averaged particle temperature (red), volume-averaged oxygen mass fraction (olive), total devolatilisation rate (blue), char conversion rate (orange) and total rates of metaplast species (grey, dashed line) for the case with $d_p = 50$ µm, $T = 1400$ K and different oxygen concentrations. (For interpretation of the references to colour in this figure legend, the reader is referred to the web version of this article.)

overlap shifts to earlier times and the duration of the overlap region becomes considerably shorter. This behaviour is primarily controlled by the second stage of devolatilisation (brown arrow). At low oxygen concentration ($X_{O_2} = 0.05$), the second stage lasts approximately 11 ms, whereas at high oxygen concentration ($X_{O_2} = 0.70$) it is reduced to about 2.5 ms. The difference in these time scales arises from the start of homogeneous gas phase reactions, shown by the strong increase of max(T_g) and decrease in oxygen concentration for $X_{O_2} = 70\%$. As mentioned earlier, the heat released from these reactions increases the particle temperature, thereby promoting further volatile release. Higher oxygen concentrations make such homogeneous reactions more likely and cause them to start earlier. Additional evidence supporting this behaviour is found in the first stage of devolatilisation (grey arrow). For both cases shown in Fig. 5, the first devolatilisation stage is independent of oxygen concentration. It ends at $t = 3$ ms in both cases, as the initial heating conditions are the same.

Another difference can be observed in the third devolatilisation stage, during which the remaining metaplast species are converted. For the case with $X_{O_2} = 0.05$, the release is very slow and stabilises at a rate of approximately $1{\cdot}10^3$ kg/(m^3 s). In the case of $X_{O_2} = 0.70$, the devolatilisation rate is dominated by the release of metaplast species between $t = 4.5$ and 5.5 ms. During this period, an overlap between second and third stages of devolatilisation is found. After the second devolatilisation stage, only metaplast species continue to be converted, indicated by a slow decline over time. This behaviour can once again be attributed to particle temperature, as higher temperatures accelerate the conversion of metaplast species.

Furthermore, the faster completion of the second devolatilisation stage at $X_{O_2} = 0.7$ results in an earlier beginning of the char conversion phase. Consequently, the fraction to start the overlap (Y_{OL}) decreases from 92.41 to 72.99% with increasing oxygen concentration due to the steeper and more rapid progression of devolatilisation, which in turn leads to an earlier and more pronounced start of char conversion.

4.3. Variation of ambient gas temperature

Fig. 6 compares the same quantities as in the previous sections, now for $d_p = 50\,\mu$m, $X_{O_2} = 0.21$ and $T = \{1000\,\text{K}, 1800\,\text{K}\}$.

A similar trend, including Fig. 4 at $T = 1400$ K, is observed for variations in ambient temperature, analogous to the effect of changing oxygen concentration. Increasing the ambient temperature shifts the beginning of the overlap from $t = 12.1$ ms for $T = 1000$ K to $t = 3.7$ ms for $T = 1800$ K. At the same time, the overlap region becomes shorter with higher ambient temperatures. This behaviour is due to the strong temperature dependence of the devolatilisation and char conversion processes. At lower ambient temperatures, as shown in Fig. 6 (top), particle heating is much slower, resulting in slower internal conversion of COAL1, COAL2, and COAL3 and consequently slower release of volatile species. The first (grey arrow) and second (brown arrow) stages of devolatilisation are therefore more pronounced and extended, with the first stage lasting approx. $t = 7.2$ ms and the second stage around $t = 12.8$ ms and longer. Due to the low temperature, the third stage of devolatilisation proceeds very slowly and is not visible within the observed time period up to $t = 20$ ms.

Increasing the ambient temperature compresses these stages into a shorter time period, see Fig. 6 (bottom). At $T = 1800$ K, the stages of devolatilisation are completed by $t = 1.9$ ms and $t = 8.05$ ms, respectively, indicating that an 80% increase in ambient temperature reduces the time for the first and second stages of devolatilisation by 60%. Moreover, the conversion of metaplast species is significantly enhanced at higher temperatures, leading to the third stage of devolatilisation overlapping with the second stage from $t = 4.5$ to 8 ms and continuing until the end of the observed time period. The conversion rates of metaplast species to light gases proceed very fast, as the rate constants, while inherently slow, are greatly accelerated by the exponential dependence on temperature.

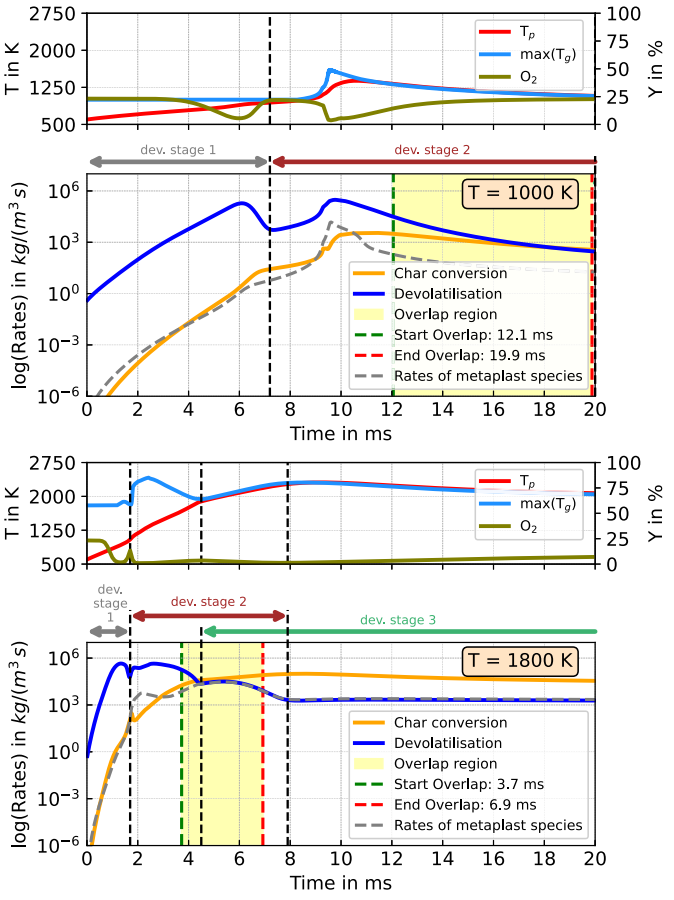

Fig. 6. Temporal evolution of maximum gas phase temperature (light-blue), volume-averaged particle temperature (red), volume-averaged oxygen mass fraction (olive), total devolatilisation rate (blue), char conversion rate (orange) and total rates of metaplast species (grey, dashed line) for the case with $d_p = 50\,\mu$m, $X_{O_2} = 0.21$ and various ambient temperatures. (For interpretation of the references to colour in this figure legend, the reader is referred to the web version of this article.)

Similar to the previous observations for cases with varying oxygen concentration, homogeneous gas phase reactions occur at the beginning of the second devolatilisation stage, resulting in a stronger increase in particle temperature and a reduction of the oxygen concentration to near-zero. For the $T = 1800$ K case, the overlap between the second and third stages is more pronounced, resulting in a further change in the slope of the particle temperature profile until the slow third stage becomes dominant, which allows the oxygen to slowly re-enter the particle. The re-entry of oxygen also occurs for the $T = 1000$ K case.

4.4. Variation of particle diameter

Fig. 7 compares the same quantities as in the previous sections, here, $d_p = \{25\,\mu\text{m}, 100\,\mu\text{m}, 150\,\mu\text{m}\}$, at an ambient temperature of $T = 1400$ K and an ambient oxygen concentration of $X_{O_2} = 0.21$.

Increasing the particle diameter while keeping all other parameters constant primarily affects the particle heating rate and consequently, the particle temperature. As a result, for larger d_p, the start of the process overlap (yellow background) shifts toward later times, while the overlap region simultaneously becomes wider. The coupled effects (as previously observed) of the first, second and third stages of devolatilisation with oxygen concentration and particle temperature can also be observed in this case. The maximum particle temperature differs among the three cases due to variations in particle mass and consequently, the amount of volatile gases released. Larger particles contain

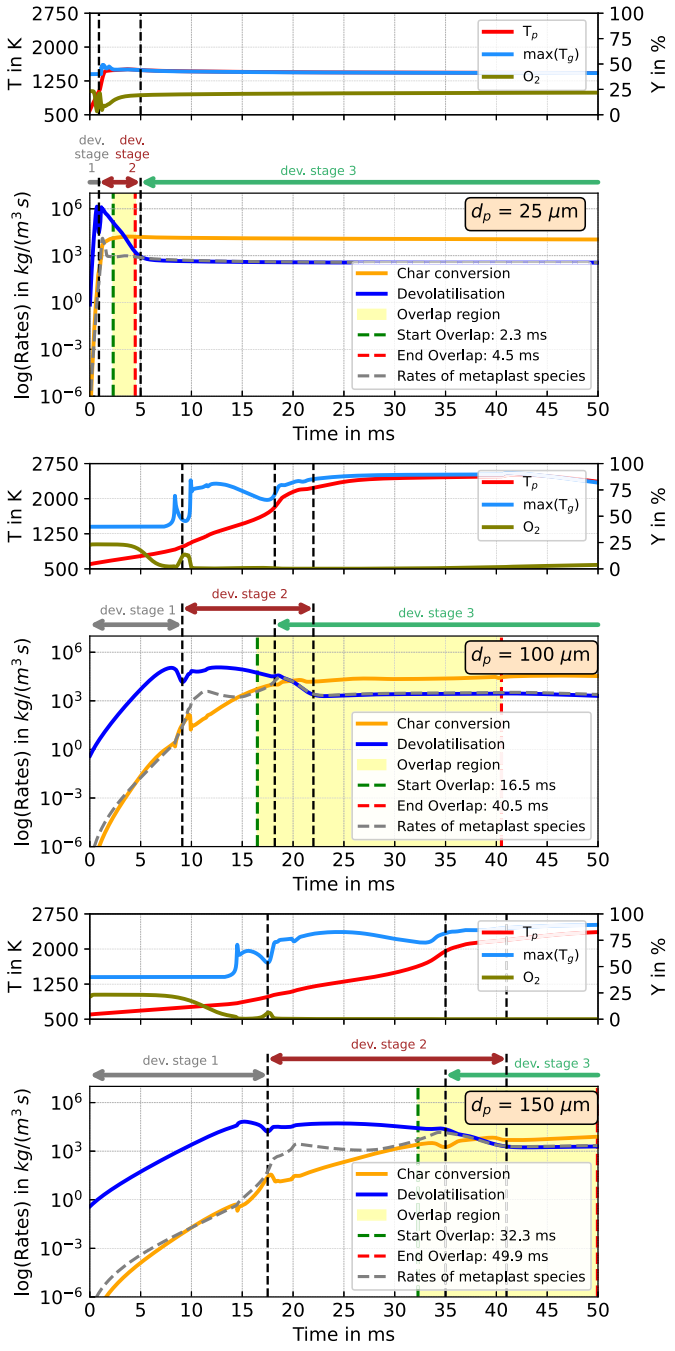

Fig. 7. Temporal evolution of maximum gas phase temperature (light-blue), volume-averaged particle temperature (red), volume-averaged oxygen mass fraction (olive), total devolatilisation rate (blue), char conversion rate (orange) and total rates of metaplast species (grey, dashed line) for the case with $d_p = \{25, 100, 150\}$ μm at $X_{O_2} = 0.21$ and $T = 1400$ K. (For interpretation of the references to colour in this figure legend, the reader is referred to the web version of this article.)

more embedded volatiles, leading to prolonged gas phase combustion and therefore, higher particle temperatures.

An additional observation is the more pronounced overlap between the second and third devolatilisation stages with increasing particle diameter, due to the higher final temperature reached. Moreover, a local maximum in the char conversion rate is observed at the transition between the first and second devolatilisation stages for $d_p \geq 100$ μm. Due to the larger particle diameter and the slower transition caused by a reduced heating rate, oxygen can re-enter the particle, thereby enhancing the char conversion rate.

4.5. Fraction of volatile mass released Y_{OL}

The fractions of volatile mass released at the start of the overlap for all investigated cases are summarised in Table 4. The results reveal a clear trend that increasing the ambient temperature, oxygen concentration and/or particle diameter leads to a lower Y_{OL}.

However, two outliers can be identified for particle sizes of $d_p = 125$ and 150 μm under the conditions of $T = 1000$ K and $X_{O_2} = 0.21$ (highlighted in blue in Table 4). Under these specific conditions, the relatively large particle diameter and low gas phase temperature result in a low heating rate, causing the particle to heat up slowly. This gradual heating leads to a slow and continuous release of volatile gases, as previously discussed in Section 4.4. Moreover, under these conditions, the oxygen concentration remains sufficient due to the lower devolatisation rate and consequently less displacement of oxygen within the particle, which allows the char conversion process to proceed. The combination of a slow volatile release and the concurrent potential for char conversion in the presence of oxygen, leads to competing rates between devolatilisation and char conversion, and therefore earlier start of the overlap or lower value of Y_{OL}.

Varying the oxygen concentration in either direction results in a smaller overlap region. A lower oxygen concentration suppresses the char conversion process, leading to a reduced overlap. Conversely, increasing the oxygen concentration enhances the char conversion rate but also raises the particle temperature, which accelerates the release of volatile species. Consequently, for this case, the relationship $Y_{OL,O_2=0.70} > Y_{OL,O_2=0.21}$ but $Y_{OL,O_2=0.70} < Y_{OL,O_2=0.05}$ arises due to the influence of char conversion.

Increasing or decreasing the oxygen concentration or ambient temperature shifts the balance toward conditions more favourable for devolatilisation.

To summarise the results in Table 4, for small particle sizes ($d_p \leq 100$ μm) under low-oxygen (and partially air) conditions and mostly independent of temperature, it can be assumed with reasonable accuracy that the devolatilisation and char conversion processes are nearly

Table 4
Overlap fraction Y_{OL} in % for various particle diameters d_p at different ambient temperatures T and oxygen concentrations X_{O_2}.

$d_p = 25$ μm	$T = 1000$ K	$T = 1400$ K	$T = 1800$ K
$X_{O_2} = 0.05$	98.49	94.72	89.13
$X_{O_2} = 0.21$	97.26	90.69	84.02
$X_{O_2} = 0.70$	92.88	81.78	75.33
$d_p = 50$ μm	$T = 1000$ K	$T = 1400$ K	$T = 1800$ K
$X_{O_2} = 0.05$	97.68	92.41	84.53
$X_{O_2} = 0.21$	94.29	83.49	76.81
$X_{O_2} = 0.70$	75.97	72.99	65.82
$d_p = 100$ μm	$T = 1000$ K	$T = 1400$ K	$T = 1800$ K
$X_{O_2} = 0.05$	95.18	85.34	84.49
$X_{O_2} = 0.21$	82.15	76.01	75.95
$X_{O_2} = 0.70$	74.25	66.43	62.97
$d_p = 125$ μm	$T = 1000$ K	$T = 1400$ K	$T = 1800$ K
$X_{O_2} = 0.05$	89.66	82.58	82.38
$X_{O_2} = 0.21$	60.85	75.29	73.78
$X_{O_2} = 0.70$	66.78	64.43	59.71
$d_p = 150$ μm	$T = 1000$ K	$T = 1400$ K	$T = 1800$ K
$X_{O_2} = 0.05$	84.71	82.02	81.75
$X_{O_2} = 0.21$	57.71	75.05	73.04
$X_{O_2} = 0.70$	66.56	64.12	59.29

separated. Thus, the conventional assumption used in reduced-order models [29,51,52] that char conversion begins once 90% of the volatile content has been released remains valid. However, for larger particle diameters and under oxyfuel conditions with strong O_2 enrichment, char conversion begins significantly earlier, typically when only 60–75% of the volatile content has been released. In the following section, a regression model is developed to account for this variability, which can be applied in reduced-order models.

4.6. Linear regression

Table 4 presents the overlap fraction Y_{OL} for various ambient conditions of temperature $T = \{1000\,K, 1400\,K, 1800\,K\}$, oxygen concentration $X_{O_2} = \{0.05, 0.21, 0.70\}$ and particle sizes $d_p = \{25\,\mu m, 50\,\mu m, 100\,\mu m, 125\,\mu m, 150\,\mu m\}$. However, a direct application of the tabulated data in reduced-order models is impractical, therefore, a linear regression of the table has been performed to provide a simplified implementable correlation for such models.

For a base particle size of $d_p = 100\,\mu m$, a linear regression model for Y_{OL} in the form of

$$Y_{OL,d_p=100\,\mu m} = \alpha + \beta \frac{T}{T_p} + \gamma X_{O_2} \tag{25}$$

has been applied to find the regression coefficients α, β and γ with $T_p = 600\,K$. Subsequently, to couple the information of different particle sizes an average absolute deviation (AAD) approach between each dataset is applied with $d_p = 100\,\mu m$ as the base set as

$$AAD_{d_p}(\%) = \frac{1}{n}\sum_{i=1}^{n} |x_{d_p=100\,\mu m,i} - x_{d_p,i}|. \tag{26}$$

Afterwards, a differentiation between smaller and larger particle sizes needs to be performed as

$$AAD_{d_p} = \begin{cases} AAD_{d_p}(\%) \cdot \frac{1}{100\%} + 1.0 & \text{for} \quad d_p \le 100\,\mu m \\ 1.0 - AAD_{d_p}(\%) \cdot \frac{1}{100\%} & \text{for} \quad d_p > 100\,\mu m \end{cases} \tag{27}$$

Now, the AAD_{d_p} for each d_p is fitted in the form as

$$\delta = a \cdot \left(\frac{d_p}{100\,\mu m}\right)^b. \tag{28}$$

with a and b the regression coefficients of Eq. (28). The final regression equation to reproduce Table 4 is the combination of Eqs. (25) and (28) as

$$Y_{OL,reg.} = \left(103.78 - 7.043\frac{T}{T_p} - 28.94 X_{O_2}\right) \cdot 0.979 \left(\frac{d_p}{100\,\mu m}\right)^{-0.095}. \tag{29}$$

To prevent non-physical values of Y_{OL}, the value should be bounded between 0 and 100% with

$$Y_{OL,bound} = \min(\max(Y_{OL,reg.}, 0), 100). \tag{30}$$

5. Conclusions

In the present study, the overlap between the devolatilisation and char conversion processes undergone by a single coal particle has been investigated using a boundary resolved simulation approach coupled with detailed homogeneous and heterogeneous reaction kinetics. The analysis was conducted under varying gas phase (oxygen concentration and temperature) and solid phase (particle diameter) conditions. The overlap is defined as the time period during which the mass conversion rates of both processes differ by less than one order of magnitude. Moreover, the start of the overlap is expressed as the fraction of volatile mass released, denoted as Y_{OL}.

We found that the proposed criterion successfully captures the temporal overlap (reflected in the varying start times and durations of the sub-processes) while responding appropriately to changes in the initial conditions. The results show a clear trend that increasing the ambient temperature, oxygen concentration, and/or particle diameter leads to a smaller Y_{OL}. A lower Y_{OL} corresponds to earlier start of the overlap between the devolatilisation and char conversion processes, indicating that once this fraction is reached, the char conversion rate becomes comparable in magnitude to the devolatilisation rate. In this regime, both processes interact strongly and their coupling must not be neglected.

Based on the results, a linear regression for Y_{OL} was derived as a function of the surrounding gas temperature, oxygen concentration and particle diameter. This correlation can be incorporated into reduced-order models to determine the appropriate activation time for the char conversion sub-model, e.g. when Y_{OL} is reached. We note that particle conversion is modelled under quiescent conditions, with several particle properties assumed to be constant, while particle shrinkage and ash layer effects are neglected. Relaxing these assumptions may change the particle heat and mass transfer, porosity, tortuosity and effective pore diffusion, which can potentially lead to different particle conversion behaviour. Addressing and quantifying these effects is beyond the scope of the present study, but should be considered in future research.

CRediT authorship contribution statement

Tien Duc Luu: Writing – original draft, Visualization, Software, Methodology, Investigation, Formal analysis, Data curation. **Ali Shamooni:** Writing – review & editing, Software, Methodology, Investigation, Data curation. **Yichong Zhou:** Writing – review & editing, Software, Methodology, Investigation, Data curation. **Andreas Kronenburg:** Writing – review & editing, Supervision, Resources, Funding acquisition, Conceptualization. **Oliver T. Stein:** Writing – review & editing, Supervision, Resources, Project administration, Methodology, Funding acquisition, Conceptualization.

Declaration of competing interest

The authors declare that they have no known competing financial interests or personal relationships that could have appeared to influence the work reported in this paper.

Acknowledgements

The authors acknowledge the financial support of the Deutsche Forschungsgemeinschaft for project number 450158108. We acknowledge support from the state of Baden-Württemberg through bwHPC.

Data availability

Data will be made available on request.

References

[1] Smith KL, Smoot LD, Fletcher TH, Pugmire RJ. The structure and reaction processes of coal. Springer; 1994.
[2] Howard JB, Essenhigh RH. Pyrolysis of coal particles in pulverized fuel flames. Ind Eng Chem Proc Design Devel 1967;6:74–84.
[3] Khatami R, Stivers C, Joshi K, Levendis YA, Sarofim AF. Combustion behavior of single particles from three different coal ranks and from sugar cane bagasse in o_2/n_2 and o_2/CO_2 atmospheres. Combust Flame 2012;159:1253–71.
[4] Khatami R, Stivers C, Levendis YA. Ignition characteristics of single coal particles from three different ranks in o_2/n_2 and o_2/CO_2 atmospheres. Combust Flame 2012;159:3554–68.
[5] Yuan Y, Li S, Li G, Wu N, Yao Q. The transition of heterogeneous–homogeneous ignitions of dispersed coal particle streams. Combust Flame 2014;161:2458–68.
[6] Xu Y, Li S, Gao Q, Yao Q, Liu JM. Characterization on ignition and volatile combustion of dispersed coal particle streams: in situ diagnostics and transient modeling. Energy Fuels 2018;32:9850–8.
[7] Li L, Tahmasebi A, Dou J, Khoshk Rish S, Tian L, Yu J. Mechanistic investigations of particle ignition of pulverized coals: an enhanced numerical model and experimental observations. Energy Fuels 2020;34:16666–78.

[8] Annamalai K, Durbetaki P. A theory on transition of ignition phase of coal particles. Combust Flame 1977;29:193–208.
[9] Zhang T, Hu Z, Zhou Y. The determination method of the ignition modes of single coal particle with a transient coal ignition and combustion model. Combust Flame 2022;241.
[10] Edge P, Gubba SR, Ma L, Porter R, Pourkashanian M, Williams A. LES modelling of AIR and oxy-fuel pulverised coal combustion-impact on flame properties. Proc Combust Inst 2011;33:2709–16.
[11] Franchetti BM, Cavallo Marincola F, Navarro-Martinez S, Kempf AM. Large eddy simulation of a pulverised coal jet flame. Proc Combust Inst 2013;34:2419–26.
[12] Stöllinger M, Naud B, Roekaerts D, Beishuizen N, Heinz S. PDF modeling and simulations of pulverized coal combustion – part 1: theory and modeling. Combust Flame 2013;160:384–95.
[13] Hara T, Muto M, Kitano T, Kurose R, Komori S. Direct numerical simulation of a pulverized coal jet flame employing a global volatile matter reaction scheme based on detailed reaction mechanism. Combust Flame 2015;162:4391–407.
[14] Muto M, Watanabe H, Kurose R, Komori S, Balusamy S, Hochgreb S. Large-eddy simulation of pulverized coal jet flame – effect of oxygen concentration on NO formation. Fuel 2015;142:152–63.
[15] Nicolai H, Li T, Geschwindner C, di Mare F, Hasse C, Böhm B, Janicka J. Numerical investigation of pulverized coal particle group combustion using tabulated Chemistry. Proc Combust Inst 2021;38:4033–41.
[16] Chen G, Wang H, Luo K, Fan J. A DNS study of pulverized coal combustion in a hot turbulent environment: effects of particle size, mass loading and preferential concentration. Combust Flame 2023;254:112839.
[17] Wen X, Scholtissek A, van Oijen J, Bergthorson J, Hasse C. Numerical modeling of pulverized iron flames in a multidimensional hot counterflow burner. Combust Flame 2023;248:112572.
[18] Luu TD, Shamooni A, Kronenburg A, Braig D, Mich J, Nguyen B-D, Scholtissek A, Hasse C, Thäter G, Carbone M, Frohnapfel B, Stein OT. Carrier-Phase DNS of ignition and combustion of iron particles in a turbulent mixing layer. Flow Turb Combust 2024;112:1083–103.
[19] Berkel LL, Steffens P, Nicolai H, Gierth S, Debiagi P, Schneider H, Dreizler A, Hasse C. Comprehensive analysis of the effect of oxyfuel atmospheres on solid fuel combustion using large eddy simulations. Fuel 2025;380:133449.
[20] Ihme M, Pitsch H. Prediction of extinction and reignition in nonpremixed turbulent flames using a flamelet/progress variable model: 2. Application in LES of sandia flames d and e. Combust Flame 2008;155:90–107.
[21] Popp S, Hunger F, Hartl S, Messig D, Coriton B, Frank JH, Fuest F, Hasse C. LES flamelet-progress variable modeling and measurements of a turbulent partially-premixed dimethyl ether jet flame. Combust Flame 2015;162:3016–29.
[22] Watanabe J, Yamamoto K. Flamelet model for pulverized coal combustion. Proc Combust Inst 2015;35:2315–22.
[23] Watanabe J, Okazaki T, Yamamoto K, Kuramashi K, Baba A. Large-eddy simulation of pulverized coal combustion using flamelet model. Proc Combust Inst 2017;36:2155–63.
[24] Wen X, Luo Y, Wang H, Luo K, Jin H, Fan J. A three mixture fraction flamelet model for multi-stream laminar pulverized coal combustion. Proc Combust Inst 2019;37:2901–10.
[25] Rieth M, Kempf AM, Stein OT, Kronenburg A, Hasse C, Vascellari M. Evaluation of a flamelet/progress variable approach for pulverized coal combustion in a turbulent mixing layer. Proc Combust Inst 2019;37:2927–34.
[26] Nicolai H, Wen X, Miranda FC, Zabrodiec D, Massmeyer A, di Mare F, Dreizler A, Hasse C, Kneer R, Janicka J. Numerical investigation of swirl-stabilized pulverized coal flames in AIR and oxy-fuel atmospheres by means of large eddy simulation coupled with tabulated Chemistry. Fuel 2021;287:119429.
[27] Meller D, Lipkowicz T, Rieth M, Stein OT, Kronenburg A, Hasse C, Kempf AM. Numerical analysis of a turbulent pulverized coal flame using a flamelet/progress variable approach and modeling experimental artifacts. Energy Fuels 2021;35:7133–43.
[28] Zhang W, Karaca S, Wang J, Huang Z, van Oijen J. Large eddy simulation of the cambridge/sandia stratified flame withflamelet-generated manifolds: effects of non-unity lewis numbers andstretch. Combust Flame 2021;227:106–19.
[29] Luu TD, Shamooni A, Stein OT, Kronenburg A, Popp S, Nicolai H, Schneider H, Wen X, Hasse C. Flame characterisation of gas-assisted pulverised coal combustion using FPV-LES. Proc Combust Inst 2023;39:3249–58.
[30] Shamooni A, Wen X, Debiagi P, Stagni A, Gärtner JW, Zirwes T, Stein OT, Hasse C, Kronenburg A. Carrier-phase direct numerical simulation and flamelet modeling of alkali metal emissions from pulverized biomass flames. Proc Combust Inst 2024;40:105309.
[31] Zhao L, Cleary MJ, Stein OT, Kronenburg A. A two-phase MMC-LES model for pyrolysing solid particles in a turbulent flame. Combust Flame 2019;209:322–36.
[32] Vascellari M, Xu H, Hasse C. Flamelet modeling of coal particle ignition. Proc Combust Inst 2013;34:2445–52.
[33] Tufano GL, Stein OT, Kronenburg A, Gentile G, Stagni A, Frassoldati A, Faravelli T, Kempf AM, Vascellari M, Hasse C. Fully-resolved simulations of coal particle combustion using a detailed multi-step approach for heterogeneous kinetics. Fuel 2019;240:75–83.
[34] Thijs LC, van Gool CEAG, Ramaekers WJS, Kuerten JGM, van Oijen JA, de Goey LPH. Improvement of heat- and mass transfer modeling for single iron particles combustion using resolved simulations. Combust Sci Technol 2022;1:1–17.
[35] Shamooni A, Stein OT, Kronenburg A, Kempf AM, Debiagi P, Li T, Dreizler A, Böhm B, Hasse C. Fully-resolved simulations of volatile combustion and NO_x formation from single coal particles in recycled flue gas environments. Proc Combust Ins 2023;39:4529–39.
[36] Luu TD, Zhang J, Gärtner JW, Meng S, Kronenburg A, Li T, Løvås T, Stein OT. Single particle conversion of woody biomass using fully-resolved and euler–lagrange coarse-graining approaches. Fuel 2024;368:131600.
[37] Sayadi T, Farazi S, Kang S, Pitsch H. Transient multiple particle simulations of char particle combustion. Fuel 2017;199:289–98.
[38] Tufano GL, Stein OT, Wang B, Kronenburg A, Rieth M, Kempf AM. Coal particle volatile combustion and flame interaction. Part I: Characterization of Transient and Group Effects. Fuel 2018;229:262–9.
[39] Tufano GL, Stein OT, Wang B, Kronenburg A, Rieth M, Kempf AM. Coal particle volatile combustion and flame interaction. Part II: effects of particle reynolds number and turbulence. Fuel 2018;234:723–31.
[40] Sommariva S, Maffei T, Migliavacca G, Faravelli T, Ranz E. A predictive multi-step kinetic model of coal devolatilization. Fuel 2010;89:318–28.
[41] Maffei T, Khatami R, Pierucci S, Faravelli T, Ranzi E, Levendis YA. Experimental and modeling study of single coal particle combustion in o_2/n_2 and oxy-fuel (o_2/CO_2) atmospheres. Combust Flame 2013;160:2559–72.
[42] Cuoci A, Frassoldati A, Faravelli T, Ranzi E. A computational tool for the detailed kinetic modeling of laminar flames: application to c_2h_4/CH_4 coflow flames. Combust Flame 2013;160:870–86.
[43] Poinsot T, Veynante D. Theoretical and numerical combustion. 2nd ed. R.T. Edwards, Inc.; 2005.
[44] Gentile G, Debiagi P, Cuoci A, Frassoldati A, Ranzi E, Faravelli T. A computational framework for the pyrolysis of anisotropic biomass particles. Chem Eng J 2017;321:458–73.
[45] Maffei T. Kinetic model of coal combustion, [Ph.D. thesis], Politecnico Di Milano; 2013.
[46] Molina A, Shaddix CR. Ignition and devolatilization of pulverized bituminous coal particles during oxygen/carbon dioxide coal combustion. Proc Combust Inst 2007;31:1905–12.
[47] Tufano GL, Stein OT, Kronenburg A, Frassoldati A, Faravelli T, Kempf AM, Vascellari M, Hasse C. Resolved flow simulation of pulverized coal particle devolatilization and ignition in AIR- and o_2/CO_2-atmospheres. Fuel 2016;186:285–92.
[48] Murphy JJ, Shaddix CR. Combustion kinetics of coal chars in oxygen-enriched environments. Combust Flame 2006;144:710–29.
[49] Cong K, Zhang Y, Han F, Li Q. Influence of particle sizes on combustion characteristics of coal particles in oxygen-deficient atmosphere. Energy 2019;170:840–8.
[50] Cuoci A, Frassoldati A, Faravelli T, Ranzi E. OpenSMOKE++: an object-oriented framework for the numerical modeling of reactive systems with detailed kinetic mechanisms. Comput Phys Commun 2015;192:237–64.
[51] Rieth M, Kempf AM, Kronenburg A, Stein OT. Carrier-phase DNS of pulverized coal particle ignition and volatile burning in a turbulent mixing layer. Fuel 2018;212:364–74.
[52] Shamooni A, Debiagi P, Wang B, Luu TD, Stein OT, Kronenburg A, Bagheri G, Stagni A, Frassoldati A, Faravelli T, Kempf AM, Wen X, Hasse C. Carrier-phase DNS of detailed NO_x formation in early-stage pulverized coal combustion with fuel-bound nitrogen. Fuel 2021;291:119998.